CRUSTAL AND MANTLE STRUCTURE BENEATH EASTERN EURASIA FROM INVERSIONS OF FINITE-FREQUENCY BODY AND SURFACE WAVES

Yong Ren[2], Ting Yang[3], Wei Zhang[2], Yang Shen[2], Brian Covellone[2], and Xiaoping Yang[1]

Science Applications International Corporation[1] , University of Rhode Island[2], and University of Texas at Austin [3]

Sponsored by Air Force Research Laboratory

Contract No. FA8718-05-C-0017

ABSTRACT

In this project we use 3D sensitivity kernels of finite-frequency body and surface waves to develop the crustal and mantle velocity structure beneath eastern Eurasia. We have processed available broadband waveforms from both permanent and Program for the Array Seismic Studies of the Continental Lithosphere (PASSCAL) stations. Delay times are measured by waveform cross-correlation in three frequency bands for P (0.5-2.0 Hz, 0.1-0.5 Hz and 0.03-0.1Hz) and S-waves (0.1-0.2 Hz, 0.05-0.1 Hz and 0.02-0.05 Hz). The measurements from these frequency bands for P are inverted jointly to obtain P velocity models, and similarly for S. The travel times are corrected for crustal effects using frequency-dependent crustal corrections. In areas with dense stations such as Tibet, we obtain high-resolution images of the crust and upper mantle structure that lead to unexpected geological findings. A prominent low-velocity anomaly is imaged in the crust and upper mantle to at least 300 km depth beneath a north-south trending rift zone in southeast Tibet. This anomaly is above a high-angle, southeastward dipping, high-velocity anomaly that extends into the upper mantle transition zone. Previous studies have suggested that the north-south rift zones in the Tibetan plateau are shallow features formed by the eastward motion of the shallow crust that are decoupled from the mantle lithosphere by a low-viscosity lower crust. Our new tomographic images provide strong evidence for the upper mantle origin of the north-south rift zones in the Tibetan plateau and the delamination of a thickened mantle lithosphere.

To improve data sampling at shallow depths, we are developing a new method to utilize the estimated Green's functions derived from cross-correlation of ambient noise at pairs of stations. Unlike previous studies that use the estimated Green's functions to solve for phase or group velocity maps and then a point-wise S velocity structure under a one-dimensional (1D) assumption, we construct three-dimensional (3D) sensitivity kernels for the finite-frequency Green's functions. A joint inversion of finite-frequency S-waves and estimated Green's functions, which are dominated by surface waves, will be carried out to resolve both the crust and upper mantle structure. These two data sets are easily integrated since the sensitivity kernels for body waves and estimated Green's functions relate the velocity and waveform perturbations (phase delay and/or amplitude reduction) in a similar way.

In the final year of this three-year project, we will complete the P and S velocity models and use them in forward modeling and event relocation. Travel-time corrections will be computed for selected stations in relocating the ground truth (GT) events collected in eastern Eurasia, and the location results will be evaluated.

OBJECTIVES

The goal of this work is to use 3D sensitivity kernels of finite-frequency body and surface waves to develop the crustal and mantle velocity structure beneath eastern Eurasia to improve seismic calibration for nuclear explosion monitoring.

RESEARCH ACCOMPLISHED

Data

We have collected and utilized a large data set of broadband waveforms to construct the finite-frequency velocity model beneath eastern Eurasia. Figure 1 shows the distribution of the stations, including the Global Seismographic Network (GSN), Japanese F-net and JISNET, Taiwan Broadband Seismic Network, other regional seismic networks available at the Data Management Center (DMC) of the Incorporated Research Institutions for Seismology (IRIS) and elsewhere (e.g. part of the Chinese Digital Seismic Network), and available stations from PASSCAL.

We select global earthquakes in the updated Engdahl-van der Hilst-Buland (EHB) bulletins prior to 2004 and the National Earthquake Information Center (NEIC) bulletins for recent events with magnitude greater than 5.5 recorded by the seismic stations in eastern Eurasia. We use event-station paths with epicentral distances between 30° and 85°. Delay times are measured by an automated waveform cross-correlation routine based on VanDecar and Crosson (1990) in three frequency bands for P waves (0.5–2.0 Hz, 0.1–0.5 Hz and 0.03–0.1Hz) and S waves (0.1–0.2 Hz, 0.05–0.1 Hz and 0.02–0.05 Hz). The signal-to-noise-ratio threshold is set as 20 for quality control in each frequency band and the selected records are visually inspected for consistency. The signal-to-noise ratio is defined as the ratio of the peak-to-peak amplitude of the main arrival to the standard deviation of the time series in an 80-s window before the main arrival. Figure 2 shows examples of the measurements of P and S differential travel times.

To reduce the tradeoff between crustal and mantle velocity heterogeneities in seismic tomography, we remove the frequency dependent crustal correction from the teleseismic travel times by cross-correlating the impulse responses of a crust model filtered in a narrow frequency band (Yang and Shen, 2006). We use a crustal model from Sun et al. (2004) for stations in China, and CRUST2.0 (Bassin et al., 2000) for stations elsewhere to calculate the travel-time difference with respect to IASPEI91 for the three frequency bands, and apply those frequency dependent adjustments to teleseismic travel times.

High-Resolution P- and S-Velocity Models in Selected Areas

The distribution of the seismic stations in eastern Eurasia is uneven (Figure 1). In places where the stations are dense, we carry out detailed data analyses to obtain high-resolution P- and S-velocity models. In addition to collecting data needed for the continental-scale inversion, these detailed studies allow us to analyze seismic data further and obtain high resolution images of the crust and mantle structure. As an example, southeastern Tibet is such a region with several PASSCAL experiments (Figure 1) for high-resolution images of the crustal and mantle structure to provide constraints on the continental collision and plateau building processes. We processed data from the Namche Barwa Seismic Experiment (Sol et al., 2007), which deployed a 50-station broadband array and a 20-element short-period array in southeastern Tibet during 2003–2004. Data from the GSN station LSA, which is located close to this temporary network, are also included in this study. Following the data processing method outlined above, we obtained 44,000 P and 19,500 S delay times, which are then utilized to invert for spatial variations in P- and S-wave velocity perturbations according to the 3-D finite frequency kernel formulation (Dahlen et al., 2000; Hung et al., 2004; Yang et al., 2006).

The model space is parameterized with a regular 3D grid of 33×33×33 centered at (93° E, 30° N), and has a dimension of 18° in longitude, 14° in latitude, and 1200 km in depth. The grid spacing is approximately 53 km in longitude, 46 km in latitude, and 40 km vertically. The inverse problem is resolved using a standard damped least square algorithm (Paige and Saunders, 1982) and the damping parameter is determined through a trade-off analysis of model norm versus variance reduction as shown in Figure 3 (Menke, 1989). We use checkerboard resolution tests with the same damping parameter as in the real data inversion to evaluate the ability of a given data coverage and inversion technique to recover crustal and mantle structures. These tests showed that structures are well recovered beneath the stations at a depth of between ~50 km and ~450 km. The minimal size of the laterally and vertically resolved structure is ~100 km.

Our results show a prominent N-S trending low-velocity anomaly at ~92°E down to at least 300 km depth (Figure 4). These structures are observed on both V_p and V_s models. We associate the high-velocity anomalies southwest and east of the north-south trending low velocity anomaly to the Indian lithosphere, which extends to ~250 km depth. We observe no evidence for a subducted Indian lithosphere at depth of 300 km or more beneath the study area. The north-south low velocity anomaly across Indus-Yarlung Suture coincides strikingly with a rift on the surface at southeastern Tibet (e.g., Tapponnier and Molnar, 1977; Armijo et al., 1986; Yin, 2000) and is above a high-angle, southeastward dipping, high-velocity anomaly that extends into the upper mantle transition zone, as shown on the cross-sections (Figure 4c). We associate the high-angle dipping, high-velocity anomaly to a sunken delaminated mantle lithosphere since its post-collisional thickening and the detachment of the mantle lithosphere can give way to asthenospheric upwelling that we associate to the north-south trending low velocity structure in our tomographic models. This mantle upwelling can thus weaken the overlying crust, localize and initiate the rifts observed on the surface in the Tibetan Plateau, at least in the region near the Eastern Himalayan Syntaxis. The observations suggest an upper mantle origin of the rift zones and that delamination plays a key role in the process (Yong and Shen, 2007), contrary to previous studies which argued that the north-south rift zones in the Tibetan plateau are shallow features, formed by the eastward motion of the shallow crust decoupled from the mantle lithosphere by a low-viscosity lower crust (e.g., Shen et al., 2001; Jiménez-Munt and Platt, 2006).

P-Velocity Model of Eastern Eurasia

The tomographic model for eastern Eurasia extends to 2500 km deep and is parameterized by a 81x81x51 grid with spacing of 1.0°, 1.25°, and 58 km in latitude, longitude and depth, respectively. As in the detailed studies, the inversion is carried out using the finite-frequency tomography methodology (Hung et al., 2004; Yang et al. 2006). We also utilize a convolutional quelling technique (Meyerholtz et al., 1989) to improve imaging in this continental-scale study.

Figure 5 shows the P-velocity anomalies at 232 km, 406 km, 580 km and 754 km depth. An inspection of the sampling of the structure beneath eastern Eurasia by the finite-frequency data finds that there is good data coverage in the depth range of 350–1500 km in most parts of the study area, but gaps exist in the shallow upper mantle and crust, except in regions with dense stations (e.g., southeast Tibet, Japan). Finite frequency surface wave tomography is necessary to obtain higher resolution in the shallow structure.

Sensitivity Kernels for Green's Functions from Ambient Noise Cross-Correlation

We utilize Green's functions derived from the cross-correlation of ambient noise at pairs of stations to image the crust and shallow mantle. Previous studies have demonstrated the efficacy of extracting information on crustal and shallow mantle structure from seismic noise to improve path coverage and spatial resolution (e.g., Shapiro and Campillo, 2004; Sabra et al., 2005; Shapiro et al., 2005; Yao et al., 2006; Yang et al., 2007; Cho et al., 2007). The fact that the estimated Green's function is based on cross-correlation makes it straightforward to adapt this type of measurement to the frequency-dependent phase-delay anomalies. Unlike previous studies that use the estimated Green's functions to solve for phase or group velocity maps and then a point-wise S velocity structure under a 1D assumption (e.g., Yao et al., 2006; Yang et al., 2007; Cho et al., 2007), we construct 3D sensitivity kernels for the finite-frequency Green's functions. Figure 6 shows the travel-time (phase-delay) sensitivity kernels for a Green's function corresponding to the estimate from the cross-correlation of vertical records at two stations separated by ~900 km. The dominant period of the seismic wave is ~10 s. The kernels are calculated using the scattering integral method (Zhao et al., 2005; Zhang et al., 2007). The reference velocity model in this figure is AK135, but any 3D heterogeneous model can be used since synthetic waveforms are computed by finite-difference full-waveform simulation. The kernel shows an approximately 200 km wide elliptical area of strong sensitivity on the horizontal slice at 18 km depth. Along the ray path the sensitivity is a local minimum, but non-zero. This general pattern of sensitivity is similar to that of Rayleigh waves from earthquakes in previous studies using semi-analytical solutions or normal modes (Zhou et al., 2005; Zhao and Jordan, 2006). A joint inversion of finite-frequency S-waves and estimated Green's functions will be carried out to resolve both the crust and upper mantle structure.

Model Validation by Ground-Truth Event Relocation

Our database also consists of a large number of GT events with location uncertainties better than 5 km (GT0-GT5) for model validation. Stations are selected to compute travel time corrections from the finite-frequency model for GT event relocation to assess location improvements. The final P and S velocity models will be used in calculating relative travel-time corrections from the kernels, and the GT events will be relocated and compared with and without the corrections.

CONCLUSIONS AND RECOMMENDATIONS

We have created a large data set of broadband waveforms and used cross-correlation to measure P- and S-wave travel-time delays at several frequency bands, which are then utilized to invert for spatial variations in P and S-wave-speed perturbations according to the 3-D finite frequency kernel formulation. We have carried out both detailed and large-scale tomographic studies and have obtained velocity models that provide new insights into geological processes. We have calculated the 3D sensitivity kernels for Green's functions derived from the cross-correlation of ambient noise at pairs of stations. A joint inversion of finite-frequency S-waves and estimated Green's functions will be carried out to resolve the crust and shallow mantle structure and reduce the tradeoff between shallow and deep velocity anomalies. The independent 3D P and S velocity models will be used in improving seismic calibration in Eurasia.

REFERENCES

Armijo, R., P. Tapponnier, J. P. Mercier, and T. Han (1986). Quaternary extension in southern Tibet, *J. Geophys. Res.* 91: 13,803–13,872.

Bassin, C., G. Laske, and G. Masters (2000). The current limits of resolution for surface wave tomography in North America, *EOS, Trans. Am. Geophys. Un.* 81: F897.

Cho, K. H., R. B. Herrmann, C. J. Ammon, K. Lee (2007). Imaging the upper crust of the Korea Peninsula by surface-wave tomography, *Bull. Seism. Soc. Am*. 97 (1B): 198–207, doi: 10.1785/0120060096.

Dahlen, F.A., Hung, S.-H., & Nolet, G. (2000). Fréchet kernels for finite frequency traveltimes-I. Theory, *Geophys. J. Int*, 141: 157–174.

Hung, S-H ,Y. Shen, and L.-Y. Chiao (2004). Imaging seismic velocity structure beneath the Iceland hot spot: A finite frequency approach, *J. Geophy. Res.* 109: doi: 10.1029/2003JB002889.

Jimenez-Munt, I., and J.P. Platt (2006). Influence of mantle dynamics on the topographic evolution of the Tibetan plateau: Results from numerical modeling, *Tectonics* 25: TC6002, doi:10.1029/2006TC001963.

Menke, W. (1989), *Geophysical data analysis: Discrete Inverse Theory*, Academic, San Diego, Calif.

Meyerholtz, K. A., G. L. Pavlis, and S. A Szpakowski (1989). Convolutional quelling in seismic tomography, *Geophysics* 54: 570–580.

Paige, C. C., and M. A. Saunders (1982). LSQR: An algorithm for sparse linear-equations and sparse least-squares, *Trans. Math. Software* 8: 43–71.

Sabra, K. G., P. Gerstoft, P. Roux, and W. A. Kuperman (2005). Extracting time-domain Green's function estimates from ambient seismic noise, *Geophys. Res. Lett.* 32: L03310, doi: 10.1029/2004GL021862.

Shapiro, N. M. and M. Campillo (2004). Emergence of broadband Rayleigh waves from correlations of the ambient seismic noise, *Geophys. Res. Lett.* 31: L07614, doi: 10.1029/2004GLL019491.

Shapiro, N. M., M. Campillo, L. Stehly, and M. H. Ritzwoller (2005). High-resolution surface-wave tomography from ambient seismic noise, *Science* 207: 1615–1618.

Shen, F., L. Royden, and B. C. Burchfiel (2001). Large-scale crustal deformation of the Tibetan plateau, *J. Geophys. Res*. 106 (B4): 6793–6816.

Sol, S., A. Meltzer, R. Burgmann, R. D. van der Hilst, R. King, Z. Chen, P. O. Koons, E. Lev, Y. P. Liu, P. K. Zeitler, X. Zhang, J. Zhang, and B. Zurek (2007). Geodynamics of the southeastern Tibetan Plateau from seismic anisotropy and geodesy, *Geology* 35: 563–566, doi:10.1130/G23408A.1.

Sun, Y., L. Xu, S. Kuleli, F. D. Morgan, and M. N. Toksoz (2004) Adaptive moving window method for 3-D P-velocity tomography and its application in China. *Bull. Seism. Soc. Am.* 94: (2) 740–746.

Tapponnier, P. and P. Molnar (1977). Active faulting and tectonics of China, *J. Geophys. Res.* 82: 2905–2930.

VanDecar, J. C., and R. S. Crosson (1990), Determination of teleseismic relative phase arrival times using multi-channel cross-correlation and least squares, *Bull. Seismol. Soc. Am.* 80: 150–169.

Yang, T. and Y. Shen (2006), Frequency dependent crustal correction for finite frequency seismic tomography, *Bull. Seism. Soc. Am.* 96: (6), 2441–2448, doi:10.1785/0120060038.

Yang, T., Y. Shen, S. van der Lee, S. C. Solomon, and S. H. Hung (2006). Upper mantle structure beneath the Azores hotspot from finite-frequency seismic tomography, *Earth Planet. Sci. Lett.* 250: 11–26.

Yang, Y., M. H. Ritzwoller, A.L. Levshi, and N.M. Shapiro (2007). Ambient noise Rayleigh wave tomography across Europe, *Geophys. J. Int.* 168: 259–274.

Yao, H., R. D. van der Hilst, and M. V. de Hoop (2006). Surface-wave array tomography in SE Tibet from ambient seismic noise and two-station analysis –I. Phase velocity maps, *Geophys. J. Int.* 166: 732–744, doi: 10.1111/j.1365-246X.2006.03028.x.

Yin, A. (2000). Mode of Cenozoic east-west extension in Tibet suggesting a common origin of rifts in Asia during the Indo-Asian collision, *J. Geophys. Res.* 105: 21,745–21,759.

Yong, R., and Y. Shen (2007). Tomographic evidence for a possible link between lithosphere delamination and the north-south trending rifts in Tibet, in preparation.

Zhang, Z., Y. Shen, and L. Zhao (2007), Finite-frequency sensitivity kernels for head waves, *Geophys. J. Int.*, accepted for publication.

Zhao, L., T. H. Jordan, K. B. Olsen, and P. Chen (2005). Frechet kernels for imaging regional earth structure based on three-dimensional reference models, *Bull. Seism. Soc. Am*. 95: 2066–2080.

Zhao, L. and T. H. Jordan (2006). Structural sensitivities of finite-frequency seismic waves: a full-wave approach, *Geophys. J. Int.* 165: 981–990, doi:10.1111/j.1365-246X.2006.02993.x.

Zhou, Y., F. A. Dahlen, G. Nolet, and G. Laske (2005), Finite-frequency effects in global surface-wave tomography, *Geophys. J. Int.*, 153, 1087–1111, doi:10.1111/j.1365-264X.2005.02780.x.

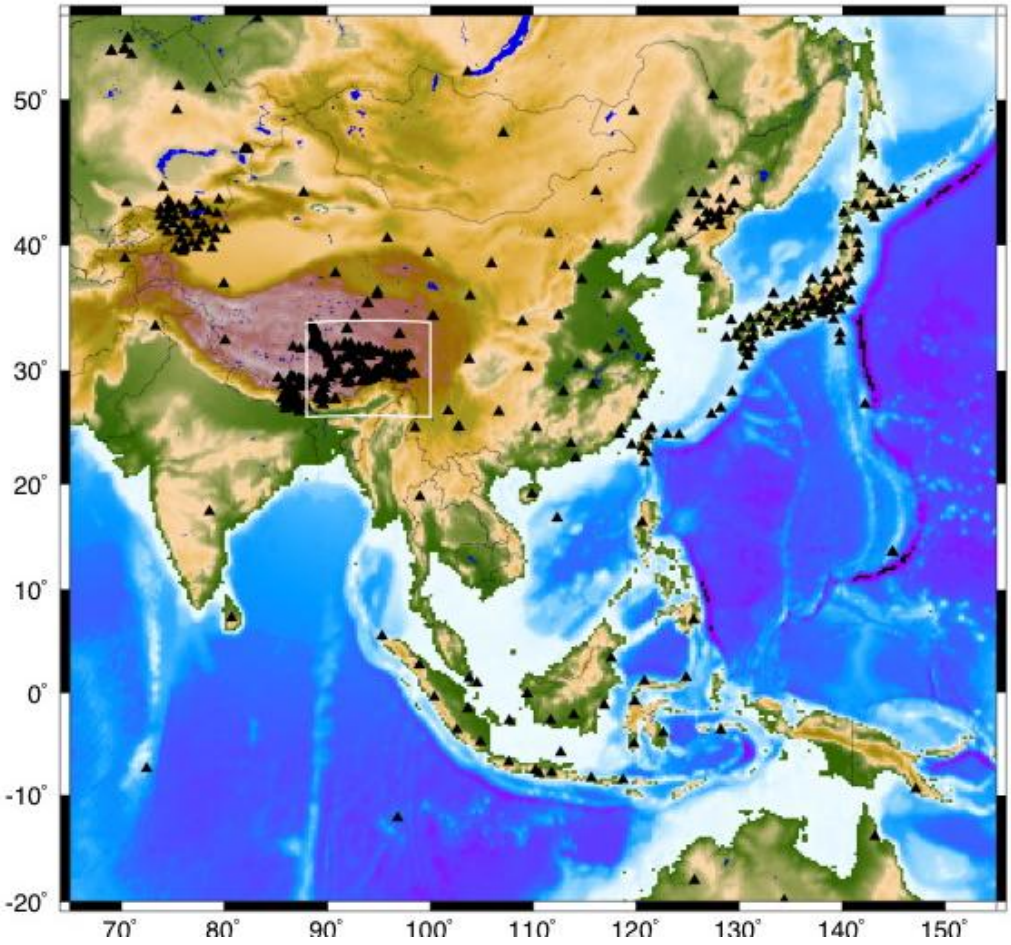

Figure 1. Topography of Eastern Eurasia and the distribution of broadband seismic stations used in this study (triangles). The box outlines a detailed study in southeastern Tibet.

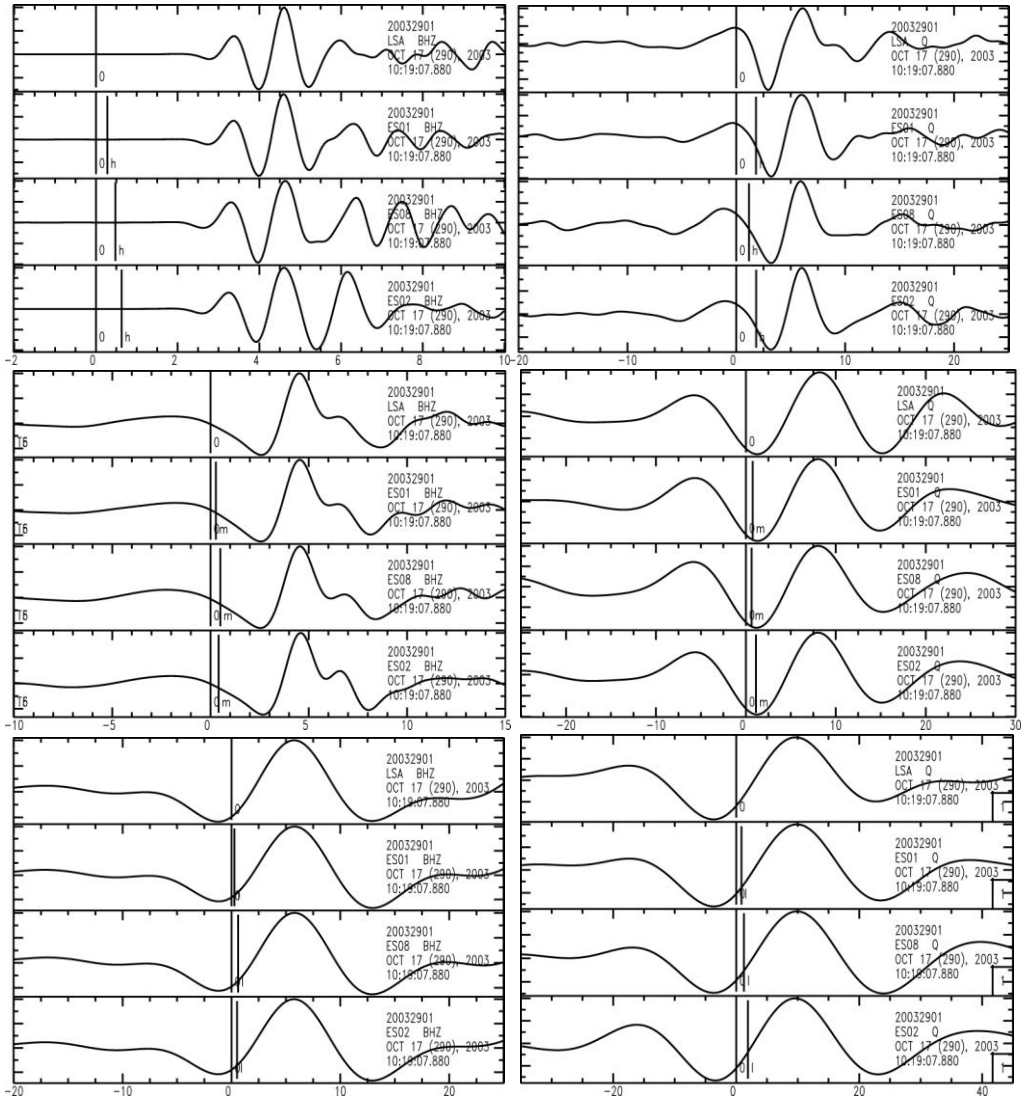

Figure 2. Examples of measurements. (left) P differential travel times in three frequency ranges: 0.5-2.0Hz, 0.1-0.5 Hz, and 0.03-0.1 Hz. (right) S differential times in three frequency ranges: 0.1-0.2 Hz, 0.05-0.1 Hz, and 0.02-0.05 Hz. The waveforms have been shifted by the delay times determined from cross-correlation (short vertical lines).

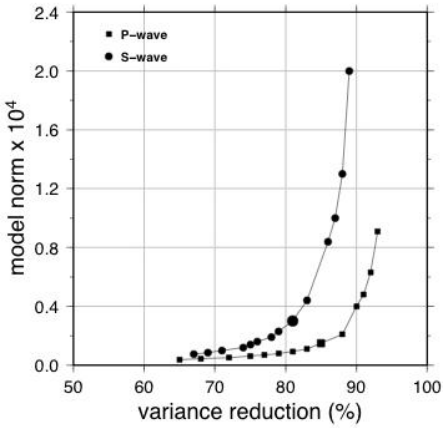

Figure 3. Trade-off between model norm and variance reduction with different damping factors for P and S velocity models. Larger symbols represent the models presented in this study. Only the high and intermediate frequencies are used here.

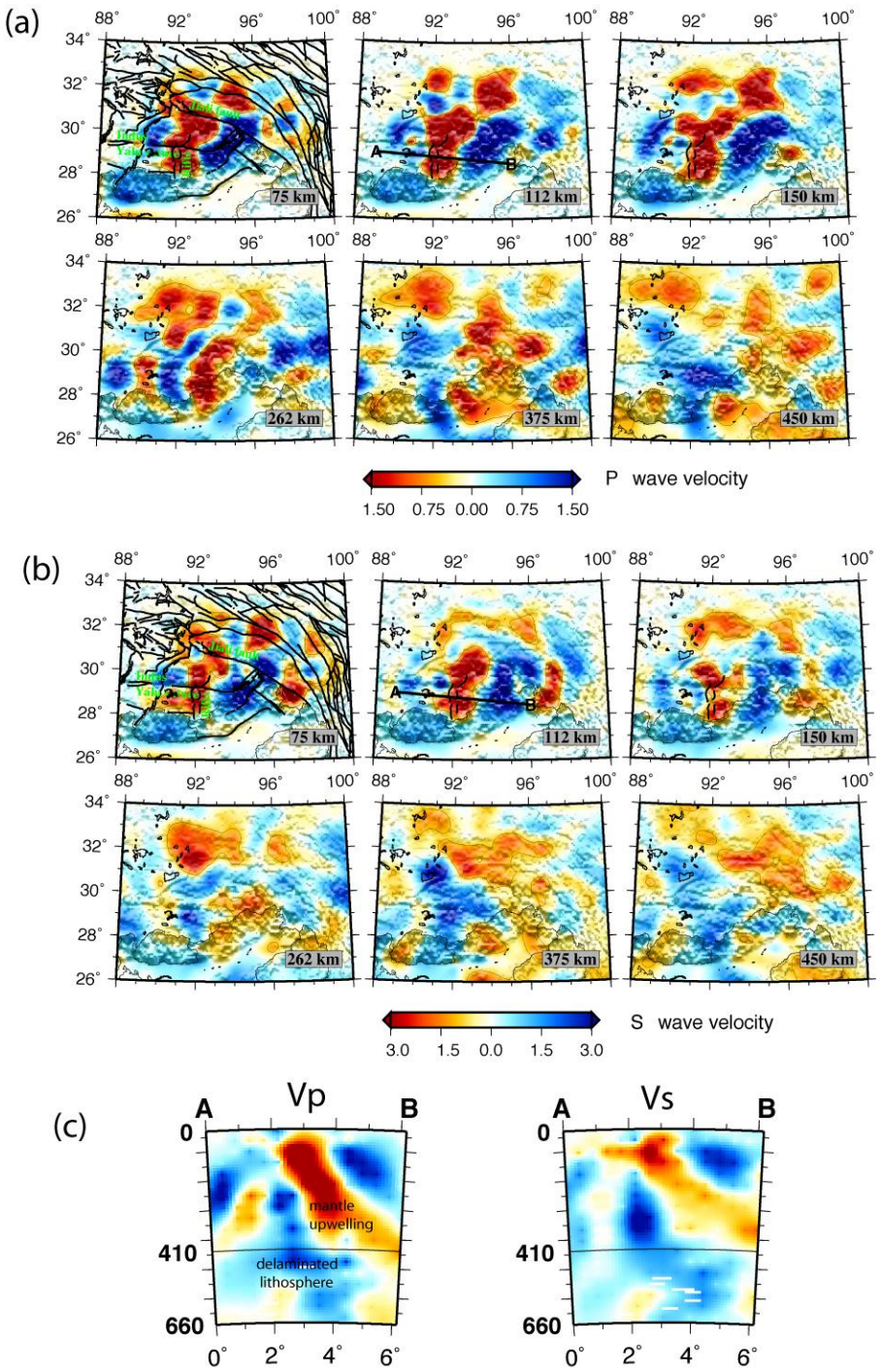

Figure 4 (a) P-velocity perturbations at several depths beneath southeastern Tibet: 75 km, 112 km, 150 km, 262 km, 375 km, and 450 km. Black lines in the 75-km horizontal slice represent the known faults. Notice the north-south trending faults (rift) coincide with a prominent north-south trending low-velocity anomaly. Line AB on the 112-km-depth image marks the location of the vertical profile in (c). (b) S-velocity perturbations at the same depths. (c) Cross-section A-B through P and S-wave tomographic models, along the Indus-Yarlung suture and across a rift in southeastern Tibet. We attribute the high-dipping-angle, high-velocity anomaly as a delaminated mantle lithosphere and the low-velocity anomaly that extends downwards beneath the rift as the upwelling of the asthenosphere to fill the gap caused by mantle delamination. The color scales for Vp and Vs are the same as in (a) and (b), respectively.

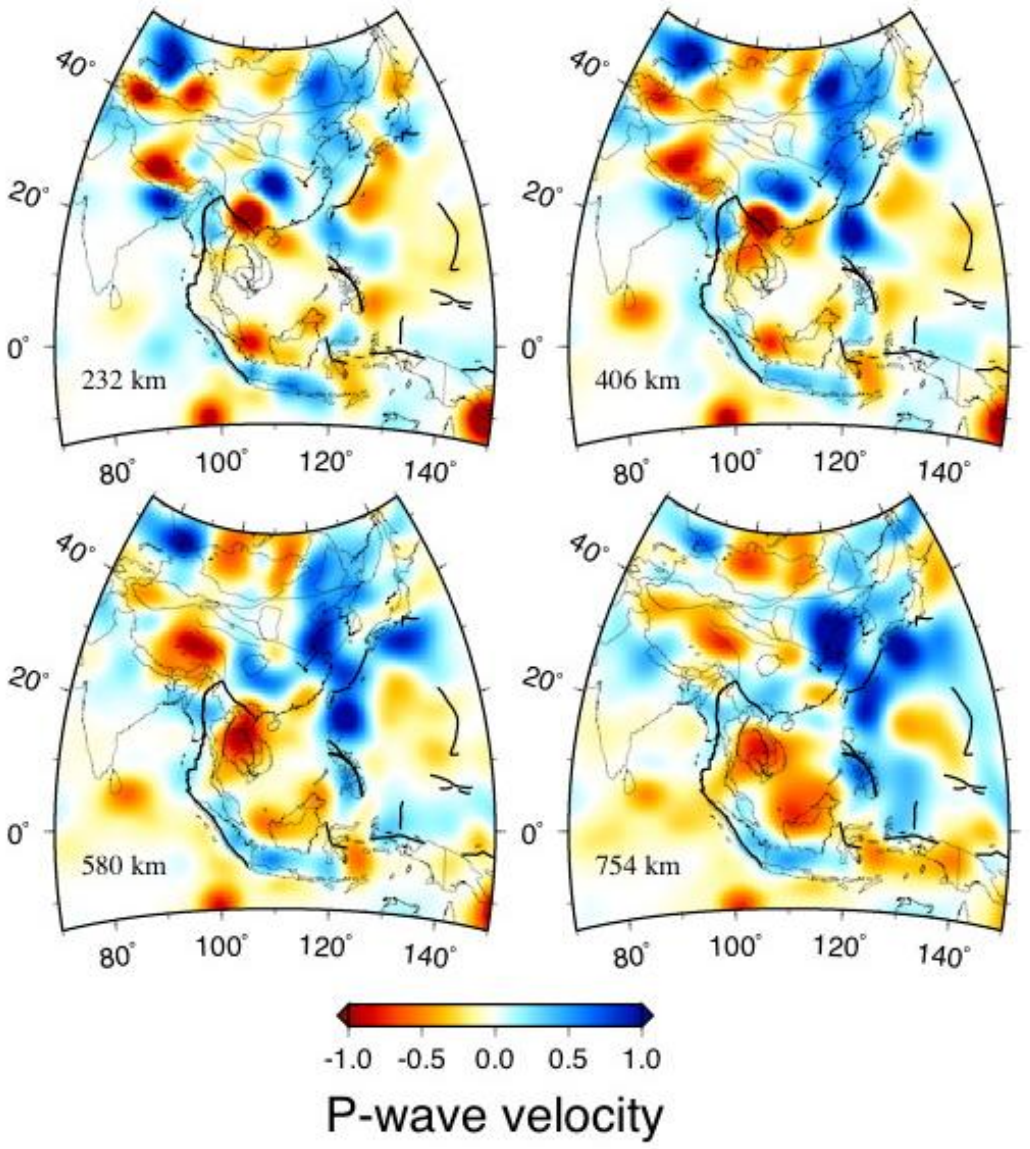

Figure 5. Horizontal slices of the tomographic model at 232 km, 406 km, 580 km and 754 km depth showing the velocity perturbation distribution in the mantle beneath Eastern Eurasia.

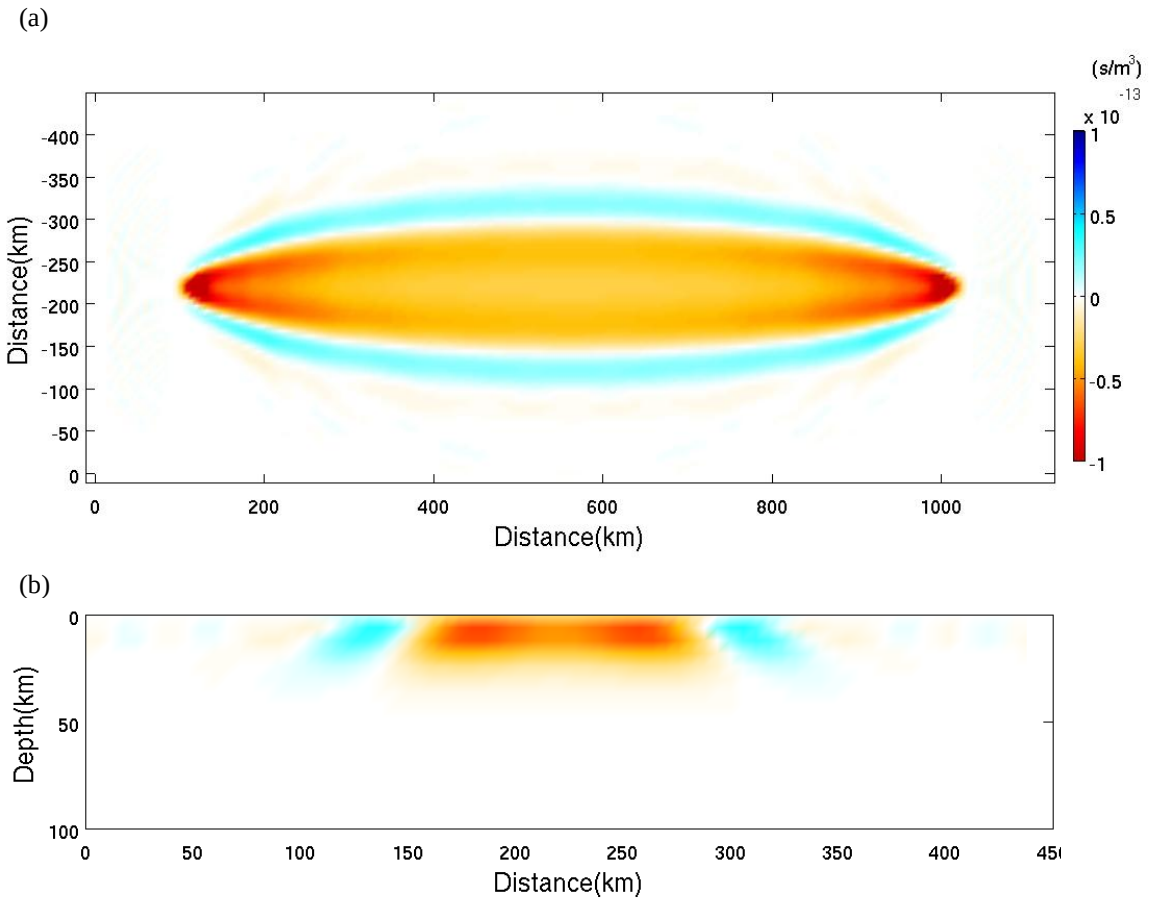

Figure 6. Travel-time (phase) sensitivity kernel to S-velocity perturbation for a 10-s Green's function for the vertical components of a pair of stations separated by ~900 km. (a) The horizontal slice of the kernel at 18 km depth. (b) The vertical slice of the kernel perpendicular to and in the middle of the station-station path. The kernel reflects primarily the finite-frequency effects of the fundamental Rayleigh waves. It is so defined that a low S-velocity perturbation in the negative (red) region results in a phase delay measured by waveform cross-correlation, while the same perturbation in the positive (blue) region results in an earlier arrival. The sensitivity is strongest near the stations and decreases toward the middle. Along the path between the two stations, the sensitivity is a local minimum but non-zero. Notice the width of the sensitivity (~200 km) is much greater than the wavelength of the 10-s surface wave (~30 km), indicating the importance of the finite-frequency effects in tomographic inversion.